Analysis of a non-LTE hypersonic spectrum of methane between 5880 and 6220 cm−1

Lyam Rolland-Roignant, Eszter Dudás, Nicolas Suas-David, Michael M. Rey, Samir Kassi, Andrei Nikitin, Robert Georges

Journal of Quantitative Spectroscopy & Radiative Transfer 347 (2025) 109656

Contents lists available at ScienceDirect

Journal of Quantitative Spectroscopy and Radiative Transfer

journal homepage: www.elsevier.com/locate/jqsrt

Analysis of a non-LTE hypersonic spectrum of methane between 5880 and 6220 cm^{-1}

Lyam Rolland-Roignant [a], Eszter Dudás [a,b], Nicolas Suas-David [a], Michaël Rey [c], Samir Kassi [d], Andrei V. Nikitin [e], Robert Georges [a,*]

[a] Institut de Physique de Rennes, UMR CNRS 6251, Université de Rennes, 35042 Rennes Cedex, France
[b] Laboratoire Collisions Agrégats Réactivité, UMR CNRS 5589, Université de Toulouse, Toulouse, France
[c] Groupe de Spectrométrie Moléculaire et Atmosphérique, UMR CNRS 7331, BP 1039, Reims Cedex 2, 51687, France
[d] Université Grenoble Alpes, CNRS, LIPhy, 38000 Grenoble, France
[e] Laboratory of Theoretical Spectroscopy, V.E. Zuev Institute of Atmospheric Optics, SB RAS, 634055 Tomsk, Russia

ARTICLE INFO

Keywords:
Infrared spectrum of methane
Hypersonic flow
CRDS
Non-LTE spectroscopy

ABSTRACT

The SMAUG device is used to thermally populate the vibrational states of the methane molecule and depopulate its rotational states through its supersonic expansion in argon. The methane molecule is probed during expansion by cavity ringdown spectroscopy (CRDS) between 5880 and 6220 cm^{-1}. The laser beam passes through both the isentropic core of the flow, characterized by a very low rotational temperature of 40.4 ± 0.8 K, and the hotter boundary layers surrounding it, which are characterized by an average rotational temperature of 364.3 ± 7.7 K. Analysis of the spectrum reveals that the vibrational population does not follow a Boltzmann distribution. A special procedure is developed to assign an effective vibrational temperature to each vibrational state, ranging from 532.4 ± 32.2 to 1112.0 ± 81.7 K for molecules in the isentropic core, and from 811.6 ± 43.1 to 851.8 ± 45.6 K for those in the shear layer. Only the first vibrational states of each methane polyad remain significantly populated leading to detectable transitions. A total of 2525 transitions from the cold gas of the isentropic core and from the warmer gas of the boundary layers are assigned from a new *ab initio* effective model and 1000 are confirmed by lower state combination differences (LSCD). Among these transitions, 718 originates from cold bands and 1807 from hot bands starting from vibrational states ν_4, ν_2 (dyad), $2\nu_4$ (pentad) and $3\nu_4$ (octad).

1. Introduction

Infrared astronomy has recently undergone considerable development, with two new space telescopes: the James Webb Space Telescope [1] and the ARIEL mission [2], which is due to launch in 2029, in addition to very high-resolution ground-based telescopes [3,4]. Modern telescopes can resolve, at least partially, the rotational structure of the spectra of the molecules present in the atmosphere of hot gaseous exoplanets, such as hot Jupiters and Neptunes whose temperature is typically of the order of 1000 K [5]. The detection of methane in the atmospheres of a significant number of hot Jupiters [1,4,6–10] is driving the production of new high-temperature, high-resolution laboratory data of this molecule, as well as the development of theoretical variational models, such as TheoReTS [11–13], ExoMol [14,15] or HITEMP [16], capable of producing synthetic spectra of methane at high temperature. Recently, a new procedure was proposed to construct "global" *ab initio* effective Hamiltonians and dipole moment operators from accurate potential and dipole moment surfaces, selected variational eigenpairs and block-diagonalization transformations [17]. This effective model, denoted as EM hereafter, was already successfully applied to methane [18] as well as to the line-by-line analysis of H_2CO [19] and CH_3F [20] high-resolution spectra. It was considered in this work for the construction of cold and hot methane transitions.

The present study focuses on the production of new spectroscopic data of methane in the tetradecad region, which is the 5th polyad of methane (P_4) located between 5120 and 6120 cm^{-1} (1.95 –1.63 μm). The cold band transitions of the tetradecad ($P_4 \leftarrow P_0$) are well known up to intermediate J values. They have been studied by various experimental techniques carried out under jet-cooled conditions [21], at liquid nitrogen temperature [22,23] or at room temperature [24–27]. Although important for astrophysical studies and to validate theoretical model predictions, high-temperature spectroscopic data of methane in

* Corresponding author.
E-mail address: robert.georges@univ-rennes.fr (R. Georges).

https://doi.org/10.1016/j.jqsrt.2025.109656
Received 10 July 2025; Received in revised form 29 August 2025; Accepted 2 September 2025
Available online 3 September 2025

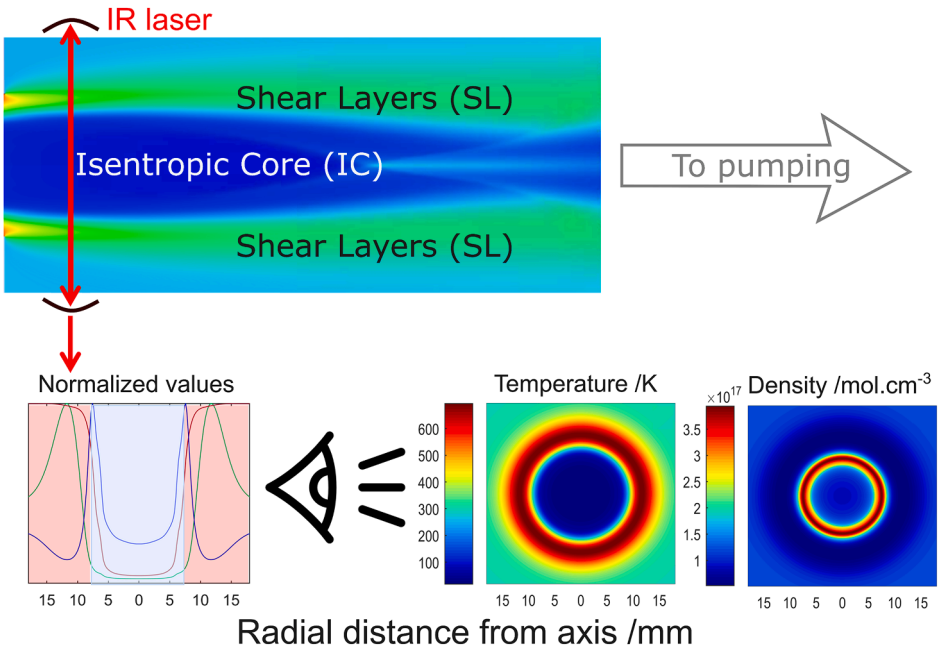

Fig. 1. CFD simulation of hypersonic expansion out of a custom-designed de Laval nozzle. Cross-sectional views of temperature and density are simulated 20 mm downstream of the nozzle outlet. The radial profiles correspond to temperature (green curve), density (blue curve) and static pressure (red curve).

this region are scarce. A laser absorption experiment at $T = 1000$ K is reported near 1.7 μm [28]. A series of Fourier transform absorption spectra were recorded between 400 and 1000 K in the 1.92–1.08 μm near-infrared region providing a useful atlas of absorption cross sections [29]. An innovative optical frequency comb double-resonance spectroscopy technique was recently used to identify a series of $3\nu_3 \leftarrow \nu_3$ hot band transitions ($P_6 \leftarrow P_2$) [18,30,31], whose contribution is of significant importance in the high temperature spectrum of the tetradecad.

The present work is part of a series of papers we have published on non-LTE spectroscopy of methane for the identification of hot bands in the tetradecad region [32–34]. It is organized as follows: the SMAUG experimental setup is briefly described in Section 2. The procedure for extracting rotational and vibrational temperatures is developed in Section 3. The approach to simulate the non-LTE spectrum is described in Section 4 and the analysis of this spectrum is explained in Section 5, before conclusion.

2. Experimental setup

The SMAUG device has been described in detail in two previous publications devoted to non-LTE spectroscopy of methane [33,34]. Briefly, an argon:methane (19:2) mixture is preheated to around 800 K before being expanded in a vacuum chamber through a small graphite de Laval nozzle, whose divergent part is specially designed to produce a collimated hypersonic flow (Mach number ~15) to avoid line broadening induced by the convective Doppler effect [35]. The flow is probed

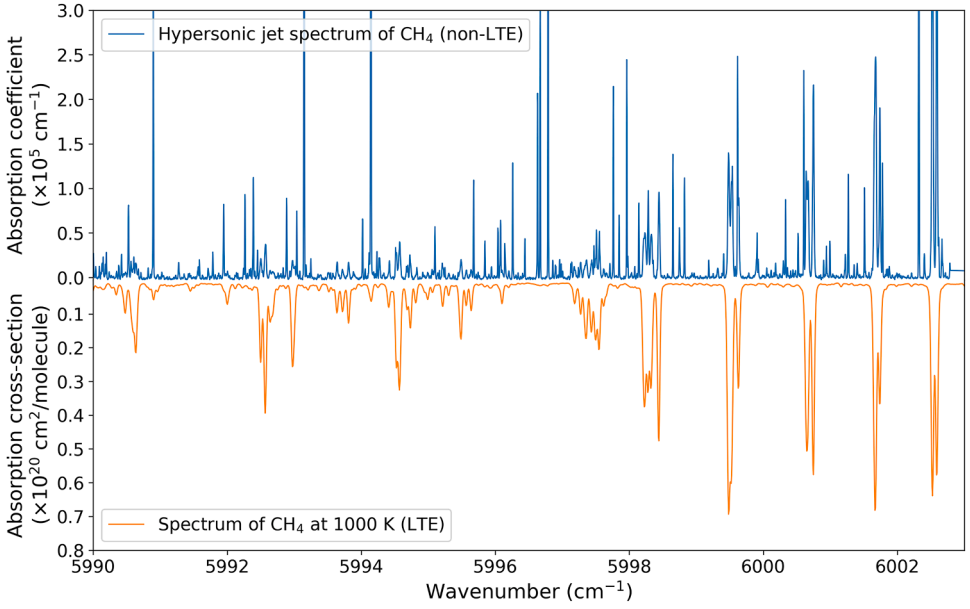

Fig. 2. Infrared spectrum of methane obtained with a Laval nozzle expansion (upper panel) compared with the spectrum recorded at 1000 K under LTE static conditions (lower panel) by Wong et al. (see Ref. [29]). The most intense lines are truncated in upper panel.

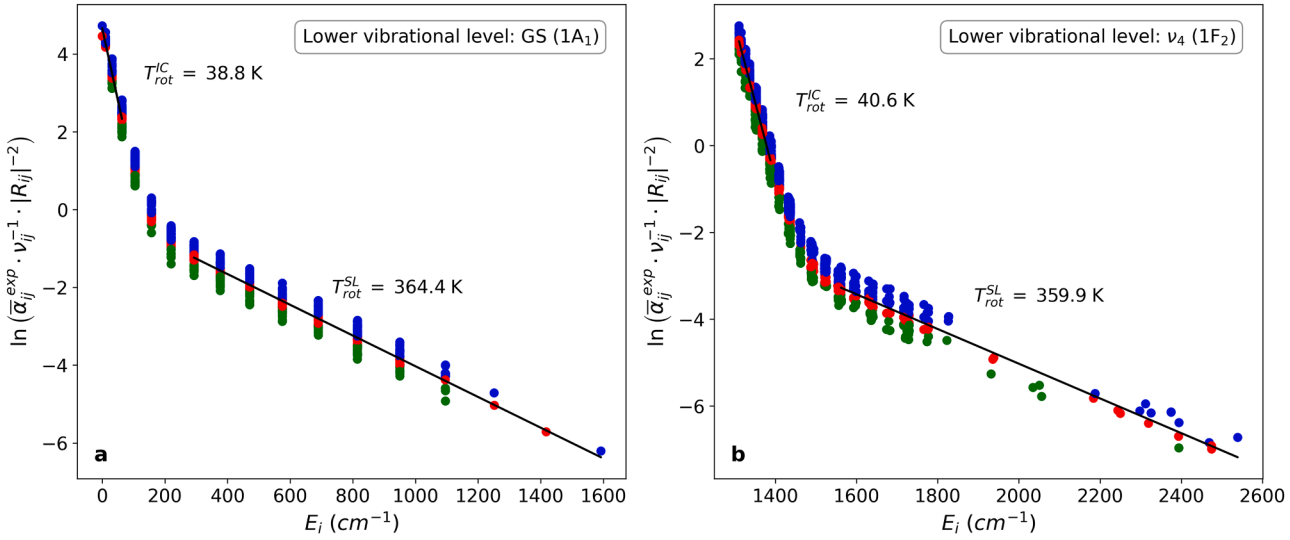

Fig. 3. Boltzmann plots constructed from rovibrational transitions starting from the ground (Panel (a)) and ν_4 (Panel (b)) states. The color code of the symbols depends on the ratio between the experimental intensity ($\overline{\alpha}_{ij}^{exp}$) and the calculated intensity ($\overline{\alpha}_{ij}^{cal}$) from the EM. Red symbols: $0.9\ \overline{\alpha}_{ij}^{cal} \leq \overline{\alpha}_{ij}^{exp} \leq 1.1\ \overline{\alpha}_{ij}^{cal}$; green symbols: $\overline{\alpha}_{ij}^{exp} < 0.9\ \overline{\alpha}_{ij}^{cal}$; blue symbols: $\overline{\alpha}_{ij}^{exp} > 1.1\ \overline{\alpha}_{ij}^{cal}$.

radially by a cavity ringdown spectrometer equipped with a series of distributed feedback (DFB) laser diodes to cover the methane absorption region between 5880 and 6220 cm^{-1}. Downstream of the nozzle throat, a boundary layer gradually develops through friction with the wall of its divergent section, so that at the nozzle outlet, the flow consists of a cold isentropic core (IC) (~40 K) surrounded by hotter shear layers (SL) (500 – 700 K), as illustrated in Fig. 1. Since CRDS is a line-of-sight absorption technique, both IC and SL contributions are present in the recorded spectra. They can be partially differentiated as the significantly higher gas temperature in the SL leads to much broader lineshapes compared to the colder IC.

The contribution of the two distinct flow regions to the recorded absorption spectrum has been investigated and showcased in previous articles [33,34]. Fig. 1 provides an overview of the laser beam pathway and the hypersonic jet structure throughout a computational fluid dynamics (CFD) simulation of the hypersonic jet ejected from the custom-designed de Laval nozzle. Panel (a) shows the axial view of the expansion, highlighting the two distinct flow regimes: the isentropic core and the surrounding shear layers, while panel (b) reveals the radial view of the jet at 2 cm downstream of the nozzle outlet, where the laser beam is located. The numerical topology of the flow shows a core free of temperature and density gradients over a radius of 5 mm. In addition, the normalized radial values for temperature (green curve), pressure (red curve) and density (blue curve) show a shift between the density peak and the temperature peak, highlighting a scenario in which the highest temperature corresponds to the lowest molecular density in the shear layer, so that its contribution is limited to the absorption spectrum.

Part of the methane spectrum obtained with the SMAUG device is shown in Fig. 2. A total of 6088 lines has been fitted with a Voigt profile. To highlight the major changes induced by rotational cooling, it is compared with a Fourier transform spectrum recorded under local thermodynamic equilibrium (LTE) conditions at 1000 K by Wong et al. [29].

3. Extraction of temperatures from the infrared spectrum

The supersonic jet is probed 2 cm downstream of the nozzle outlet. In such confined de Laval expansion, the total number of two-body collisions experienced by the molecules along the expansion is sufficiently high to allow complete rotational relaxation with translation ($T_{rot} = T_{trans}$), however the spectrum reveals that their vibrational degrees of freedom are far from completely relaxed. More precisely, our previous studies [33,34] have shown a fairly efficient depopulation of the vibrational excited states within a polyad, but an inefficient vibrational relaxation between different methane polyads. As a result, the first vibrational energy levels of each polyad, i.e. those corresponding to the vibrational states ν_4, $2\nu_4$, $3\nu_4$ etc. (and their relative sub-states), are overpopulated, resulting in an effective vibrational temperature – used as a proxy concept to characterize the population of each vibrational state – which can be even higher than the initial stagnation temperature. Before analyzing the spectrum recorded under such conditions of non-local thermodynamic equilibrium (non-LTE), it is necessary to accurately determine the rotational temperature, T_{rot}, and the various effective vibrational temperatures, $\widetilde{T}_{vib,i}$, characteristic of the population of each lower vibrational state, which may be a fundamental, overtone or combination mode.

3.1. Rotational temperatures

As they follow LTE relaxation, the IC and SL rotational temperatures are extracted from a conventional Boltzmann plot [36] (see Fig. 3), according to the following equation:

$$ln\left(\overline{\alpha}_{ij}\cdot\widetilde{\nu}_{ij}^{-1}\cdot|R_{ij}|^{-2}\right) = -\frac{E_i}{kT_{rot}^{IC/SL}} + C \tag{1}$$

Where C is a constant term; k is the Boltzmann constant; E_i (cm^{-1}) is the energy of the lower rovibrational state; $\overline{\alpha}_{ij}$ (cm^{-2}) is the integrated absorption coefficient of the rovibrational transition $j \leftarrow i$ which is directly extracted from the surface area of the corresponding absorption line; $\widetilde{\nu}_{ij}$ (cm^{-1}) is the wavenumber of the transition; $|R_{ij}|^2$ is the transition moment squared. For electric dipole transitions, $|R_{ij}|^2$ is related to the Einstein coefficient A_{ij} by:

$$|R_{ij}|^2 = \frac{3h\varepsilon_0}{16\pi^3}\frac{g_j A_{ij}}{\widetilde{\nu}_{ij}^3} \tag{2}$$

With h the Planck's constant; ε_0 the vacuum permittivity; $g_j = (2J_j+1)g_{ns}$ the statistical weight of the upper state, where J_j is the quantum number associated with the total angular momentum of the upper rovibrational state, and g_{ns} is the nuclear statistical weight equal to 5, 2, 3 for the symmetry of the upper rovibrational state A_1/A_2, E, F_1/F_2, respectively. All Einstein coefficients are taken from a line list

Table 1
Effective vibrational temperatures of the isentropic core (IC) and shear layer (SL) associated with the dyad and certain vibrational levels of the pentad. Number ***n*** is a vibrational multiplicity index and ***C*** is the vibrational symmetry. Of the 24 vibrational sublevels of the octad, only the 4 that were observed are shown in the table.

Polyad	E_{vib} (cm^{-1})	v_1	v_2	v_3	v_4	n	C	$\widetilde{T}^{IC}_{vib,i}$(K)	$\widetilde{T}^{SL}_{vib,i}$(K)
GS	0.00000	0	0	0	0	1	A_1	–	–
Dyad	1310.76150	0	0	0	1	1	F_2	865.7 ± 63.7	851.8 ± 45.6
	1533.33250	0	1	0	0	1	E	532.4 ± 32.2	811.6 ± 43.1
Pentad	2587.04375	0	0	0	2	1	A_1	1112.0 ± 81.7	–
	2614.26120	0	0	0	2	1	F_2	854.1 ± 37.8	–
	2624.61671	0	0	0	2	1	E	792.2 ± 38.9	–
	2830.31530	0	1	0	1	1	F_2	–	–
	2846.07500	0	1	0	1	1	F_1	–	–
	2916.48158	1	0	0	0	1	A_1	–	–
	3019.49280	0	0	1	0	1	F_2	–	–
	3063.64504	0	2	0	0	1	A_1	–	–
	3065.14098	0	2	0	0	1	E	–	–
Octad	3870.48560	0	0	0	3	1	F_2	1081.6 ± 44.8	–
	3909.18847	0	0	0	3	1	A_1	857.2 ± 48.5	–
	3920.51480	0	0	0	3	1	F_1	838.9 ± 45.6	–
	3930.91820	0	0	0	3	2	F_2	783.6 ± 45.6	–
	…								

produced by the effective model [17].

Two sets of absorption lines are used to access the rotational temperatures of the supersonic flow. A first set gathers all transitions starting from the vibrational ground state (cold bands), while a second set gathers the transitions starting from the vibrational level ν_4. Thus, the rotational temperatures extracted from the respective Boltzmann diagrams (see Fig. 3) are 38.8 ± 2.1 K and 40.6 ± 0.8 K for the IC, and 364.4 ± 9.4 K and 359.9 ± 16.8 K for the SL. Finally, using all the rotational temperatures extracted from the full set of assigned lines, weighted average temperatures (the weights being the inverse of the uncertainties) of 40.4 ± 0.8 K and 364.3 ± 7.7 K are used to simulate the non-LTE spectrum (see Fig. 6). The rotational temperature of the shear layer is extracted from the lines with J_i from 7 to 18, while the rotational temperature of the isentropic core is extracted from the lines with $J_i \leq 3$, once intensities have been corrected for the contribution of the hot gas in the shear layer.

The dispersion of the points observed in the Boltzmann diagrams in Fig. 3 is linked to certain inaccuracies in the measurement of the surface area of the lines. The line intensities, $\overline{\alpha}^{exp}_{ij}$, are retrieved by fitting the lines with a Voigt profile. They were compared with the line intensities, $\overline{\alpha}^{cal}_{ij}$, calculated with the effective model and adapted to the specific non-LTE conditions of the spectrum (see Sections 4 and 5). In Fig. 3, red symbols correspond to $0.9\ \overline{\alpha}^{cal}_{ij} \leq \overline{\alpha}^{exp}_{ij} \leq 1.1\ \overline{\alpha}^{cal}_{ij}$, green symbols to $\overline{\alpha}^{exp}_{ij} < 0.9\ \overline{\alpha}^{cal}_{ij}$, and blue symbols to $\overline{\alpha}^{exp}_{ij} > 1.1\ \overline{\alpha}^{cal}_{ij}$.

3.2. Effective vibrational temperatures

The different effective vibrational temperatures, $\widetilde{T}_{vib,i}$, are listed in Table 1, they are extracted from the non-LTE experimental spectrum according to a specific numerical procedure explained in detail below. In addition to our previous analyses [33,34], this new procedure involves a much larger number of rovibrational transitions gathering all the hot bands detected, which significantly improves the accuracy of the temperatures measured.

This procedure is based on Eq. (3), rewritten in the form of Eq. (4) so as to calculate LTE line intensities, $S^{LTE}_{ij}(T_0)$ at a reference temperature T_0 from the non-LTE experimental line intensities $S^{nLTE}_{ij}(T_{rot}, \widetilde{T}_{vib,i})$:

$$S^{nLTE}_{ij}(T_{rot},\ \widetilde{T}_{vib,i}) = S^{LTE}_{ij}(T_0)\frac{Q_0(T_0)}{Q_{rot}(T_{rot}) \times \widetilde{Q}_{vib}(\widetilde{T}_{vib})} \times \frac{exp\left[-c_2\left(\frac{E_{vib,i}}{\widetilde{T}_{vib,i}} + \frac{E_{rot,i}}{T_{rot}}\right)\right]}{exp\left(-c_2\frac{E_i}{T_0}\right)} \quad (3)$$

$$S^{LTE}_{ij}(T_0) \propto S^{nLTE}_{ij}(T_{rot},\ \widetilde{T}_{vib,i})\ \frac{exp\left(-c_2\frac{E_i}{T_0}\right)}{exp\left[-c_2\left(\frac{E_{vib,i}}{\widetilde{T}_{vib,i}} + \frac{E_{rot,i}}{T_{rot}}\right)\right]} \quad (4)$$

The stimulated emission has been neglected in Eqs. (3) and (4). The $S_{ij}(T_0)$ reference absorption cross sections calculated at $T_0 = 296$ K, as well as the lower energy levels, E_i, of the transitions are given by the EM. $Q_0(T_0)$ is the LTE total partition function at T_0, while $Q_{rot}(T_{rot})$ and $\widetilde{Q}_{vib}(\widetilde{T}_{vib})$ are the rotational and non-LTE vibrational partition functions, respectively. $\widetilde{Q}_{vib}(\widetilde{T}_{vib})$ is calculated using the non-LTE TIPS code, developed for non-LTE conditions (NLTE_TIPS_2021) [37,38]. In Eq. (3), $\widetilde{T}_{vib}$ refers to the total set of measured vibrational temperatures (see Table 1), while in Eqs. (3) and (4), $\widetilde{T}_{vib,i}$ refers to the specific vibrational temperature related to the population of the lower vibrational state ν_i, which may be a fundamental, overtone or combination mode. E_i denotes the lower energy level of the transition, decomposing into a vibrational and a rotational component, $E_{vib,i}$ and $E_{rot,i}$, respectively. The experimental values of the lower vibrational levels $E_{vib,i}$ are provided in Table S1, while $E_{rot,i}$ is directly obtained by $E_{rot,i} = E_i - E_{vib,i}$, where E_i is the rovibrational energy of the lower energy level calculated by our effective model (see Table S1). Finally, c_2 is the second radiation constant given by $c_2 = \frac{hc}{k} = 1.4388$ cm K, where h is the Planck constant, k is the Boltzmann constant, and c is the speed of light. Note that in Eq. (4), the ratio of partition functions has not been explicitly written because this ratio is the same for all rovibrational transitions and it is therefore not necessary to extract the temperature from the slope of a Boltzmann plot.

The procedure described below is repeated for each set of transitions starting from the same excited vibrational state. Thus, for example, the vibrational temperature $\widetilde{T}_{vib,\nu_4}$ related to the vibrational state ν_4 is derived from all observed transitions belonging to hot bands starting from ν_4. In a first stage, the rotational temperature, T_{rot}, is fixed to its extracted value (see Section 3.1). In a second stage, the effective vibrational temperature, $\widetilde{T}_{vib,i}$, is fitted in Eq. (4) until calculated line intensities correspond to the LTE line intensities $S^{LTE}_{ij}(T_0)$ at a fixed temperature T_0.

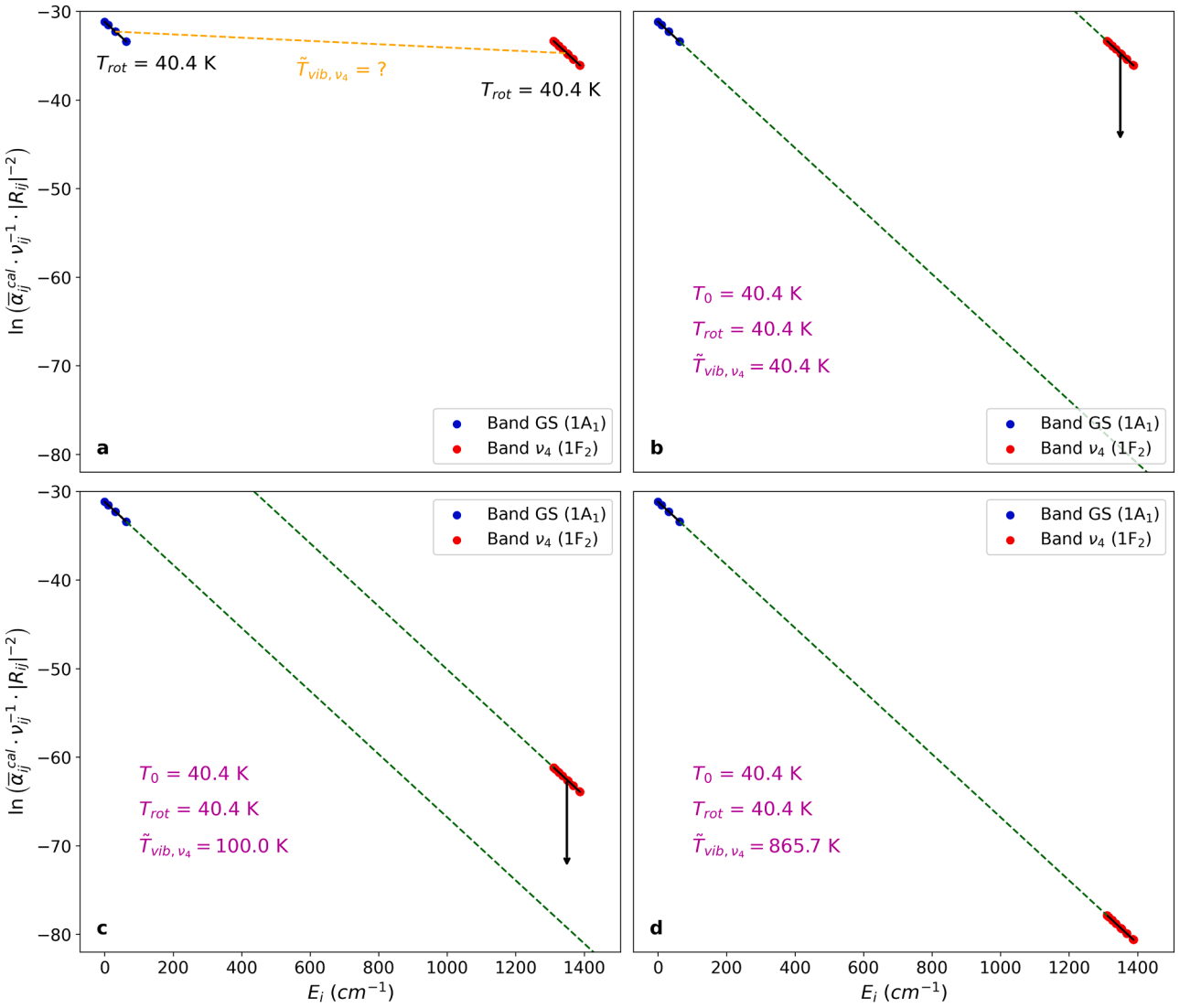

Fig. 4. Boltzmann plots obtained from simulated spectra including cold bands (blue symbols) and hot bands starting from the ν_4 vibrational state (red symbols). Panel (a): Line intensities simulated under non-LTE conditions (T_{rot} = 40.4 K, unknown $\widetilde{T}_{vib,\nu_4}$). The following three panels correspond to intensities calculated from Eq. (4) for 3 different vibrational temperatures $\widetilde{T}_{vib,\nu_4}$: Panel (b): 40.4 K; Panel (c): 100 K; Panel (d): 865.7 K, the converged vibrational temperature.

The procedure is illustrated by Fig. 4 obtained from a simulated non-LTE spectrum with a rotational temperature of 40.4 K and a supposedly "unknown" vibrational temperature $\widetilde{T}_{vib,\nu_4}$ (set at 865.7 K in this particular example). Panel (a) shows two Boltzmann plots obtained on the one hand from the cold bands corresponding to the entire recorded spectral range, and on the other hand from all the hot bands starting from the vibrational state ν_4. Only transitions corresponding to $J \leq 3$ are considered which represents several dozens of lines. However, in this simulation, a large number of data points overlap perfectly, which explains the low apparent number of transitions visible on the graphs. In panel (b), line intensities were calculated using Eq. (4) and setting $T_0 = \widetilde{T}_{vib,\nu_4} = T_{rot} = 40.4$ K. As a result, two distinct parallel lines are obtained, which clearly indicates that 40.4 K is not the correct vibrational temperature, because for an LTE spectrum, all the data points should be aligned on the same line. The calculation of the line intensity is then repeated by changing the vibrational temperature input in Eq. (4). In panel (c), the two parallel lines are closer together, indicating that the unknown temperature is closer to 100 K than to 40.4 K. Finally, in panel (d), the two parallel lines overlap, meaning that $\widetilde{T}_{vib,\nu_4} = 865.7$ K is the correct vibrational temperature, as it gives LTE line intensities $S_{ij}^{LTE}(T_0 =$ 40.4 K). This value of 865.7 K is indeed equal to the vibrational temperature $\widetilde{T}_{vib,\nu_4}$ used to produce the initial synthetic spectrum.

Fig. 5 shows Boltzmann plots calculated from the observed cold bands and the hot bands starting from ν_4. The dispersion of the points reflects an inaccuracy in the measurements of the line areas. Panel (a) reveals a strong non-LTE situation with a steep slope for the rotational temperature (extracted following the procedure described in Section 3.1) and a shallower slope for the vibrational temperature, indicating that $\widetilde{T}_{vib,\nu_4} \gg T_{rot}$. Plots showed in panel (b) were obtained by applying the procedure described above, leading to $\widetilde{T}_{vib,\nu_4} = 865.7$ K.

It can be seen from Table 1 that the vibrational states display a strong non-LTE behavior for the IC, with $\widetilde{T}^{IC}_{vib,\nu_4} > \widetilde{T}^{IC}_{vib,\nu_2}$ for the dyad (2nd polyad, P_1), $\widetilde{T}^{IC}_{vib,2\nu_4(A_1)} > \widetilde{T}^{IC}_{vib,2\nu_4(F_2)} > \widetilde{T}^{IC}_{vib,2\nu_4(E)}$ for the pentad (3rd polyad, P_2), and $\widetilde{T}^{IC}_{vib,3\nu_4(1F_2)} > \widetilde{T}^{IC}_{vib,3\nu_4(A_1)} > \widetilde{T}^{IC}_{vib,3\nu_4(F_1)} > \widetilde{T}^{IC}_{vib,3\nu_4(2F_2)}$ for the octad (4th polyad, P_3). Note that the $\nu_2+\nu_4$ (F_2,F_1), ν_1 (A_1), ν_3 (F_2) and $2\nu_2$ (A_1,E) states of the pentad are not sufficiently populated to be detected in our experiment. The same observation can be made for the states of the octad beyond the series of 4 vibrational sub-states $3\nu_4$. It is then clear that the population of the higher vibrational states in each

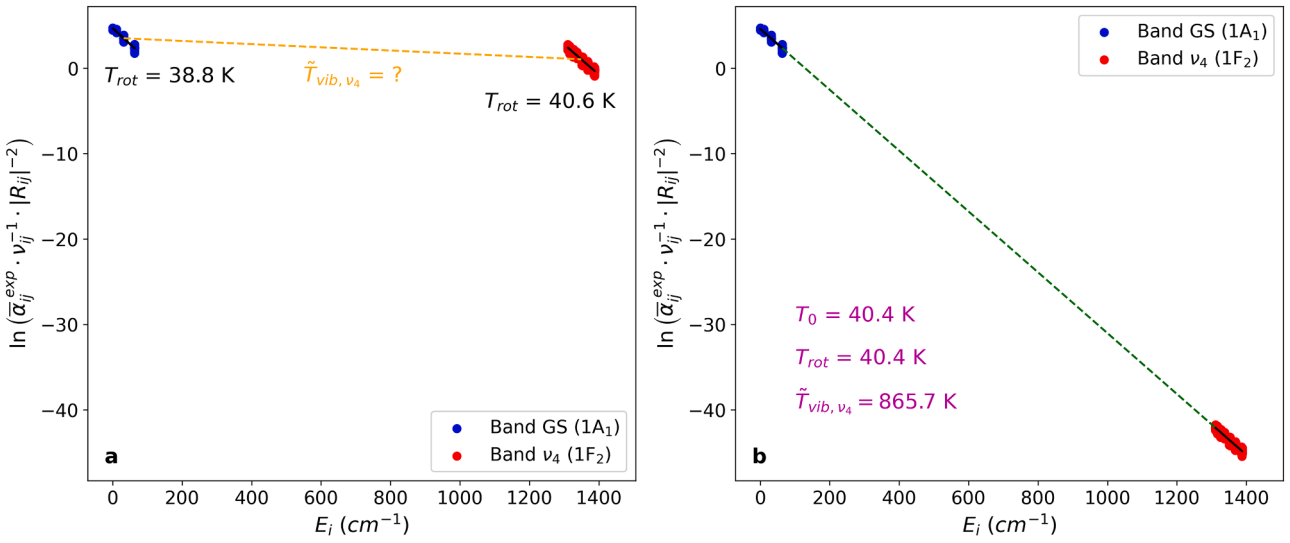

Fig. 5. Boltzmann plots obtained from the observed cold bands (blue symbols) and the hot bands starting from the ν_4 vibrational state (red symbols). Panel (a): Boltzmann plot before the procedure; panel (b): Boltzmann plot after the procedure.

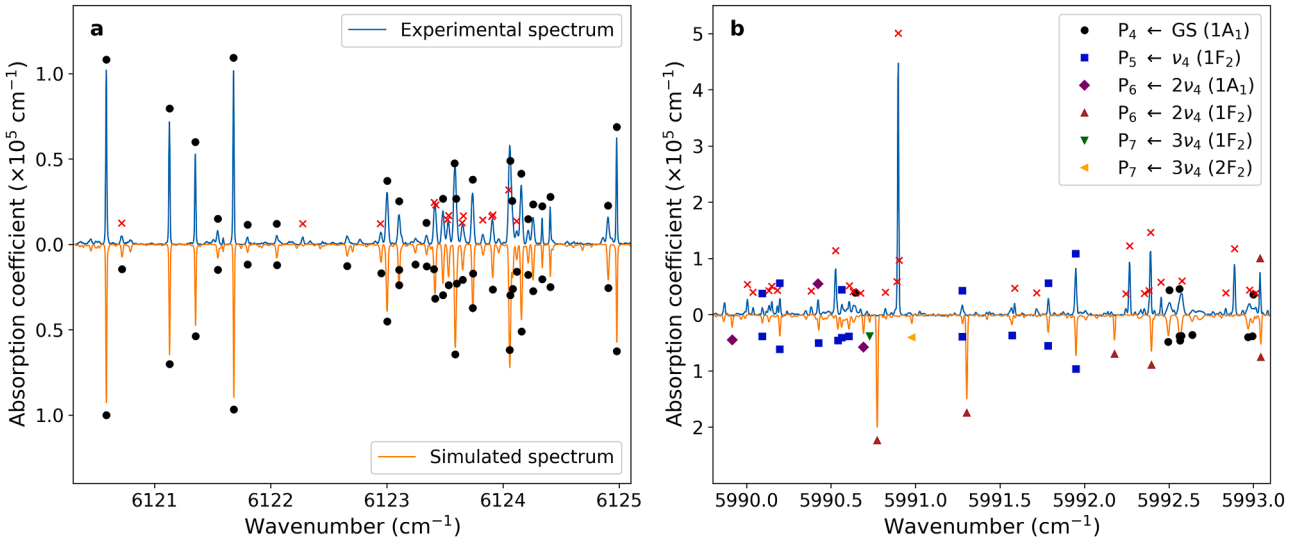

Fig. 6. Observed and simulated non-LTE spectrum of methane. Panel (a): Spectral region well reproduced by the EM. Panel (b): Hot band transitions involving higher polyads with obvious disagreements between theoretical and experimental data. Red cross symbols correspond to cases where the criteria $|\tilde{\nu}_{exp} - \tilde{\nu}_{calc}| \leq 0.01$ cm^{-1} or $0.67\ H_{ij}^{cal} \leq H_{ij}^{exp} \leq 1.33\ H_{ij}^{cal}$ are not met (see Section 5).

polyad relaxes onto their lower vibrational state(s), i.e., $\nu_4(F_2)$ for the dyad, $2\nu_4(A_1, F_2, E)$ for the pentad, and $3\nu_4(1F_2, A_1, F_1,\ 2F_2)$.

Interestingly, the shear layer exhibits a different behavior with closer vibrational temperatures, as observed for the dyad ($\tilde{T}_{vib,\nu_4}^{SL} > \sim \tilde{T}_{vib,\nu_2}^{SL}$) (see Table 1). Unfortunately, the intensities of the hot bands observed in the SL and starting from the pentad and the octad are too low to extract the corresponding vibrational temperatures. The relatively high rotational temperature ($T_{rot}^{SL} = 364.3$ K) in the SL is responsible for a dispersion of the population in many rotational energy levels, so that the intensity of the corresponding transitions falls under our detection limit.

4. Spectrum simulation

Eq. (3) is used to calculate two sets (IC and SL) of non-LTE line intensities from the LTE line intensities provided by the EM. The simulated spectrum is then obtained using Eq. (5) in which the summation symbol relates to all rovibrational transitions:

$$\alpha^{cal}(\tilde{\nu}) = \sum \left[\left(S_{ij}^{nLTE}\right)_{IC} n_{IC} G_{IC}(\tilde{\nu} - \tilde{\nu}_{ij}) + \left(S_{ij}^{nLTE}\right)_{SL} n_{SL} G_{SL}(\tilde{\nu} - \tilde{\nu}_{ij}) \right] \quad (5)$$

The line intensities are convoluted by a gaussian profile (G) with a FWHM of 0.00915 cm^{-1} and 0.01634 cm^{-1} for the IC and the SL, respectively. The molecular densities n_{IC} and n_{SL} are estimated using Eqs. (6) and (7):

$$n_{IC} = \frac{\overline{\alpha}_{ij}^{exp}}{S_{ij}^{nLTE}} \times \frac{L}{d_{IC}} \quad (6)$$

$$n_{SL} = \frac{\overline{\alpha}_{ij}^{exp}}{S_{ij}^{nLTE}} \times \frac{L}{d_{SL}} \quad (7)$$

Where $L = 800$ mm is the total length of the optical cavity and d_{IC} and d_{SL} are the lengths of the IC and SL crossed by the laser beam. $d_{IC} \approx 10$ mm and $d_{SL} \approx 10$ mm are estimated on the basis of the CFD simulations shown in Fig. 1. Only transitions with $J \leq 3$ were considered to

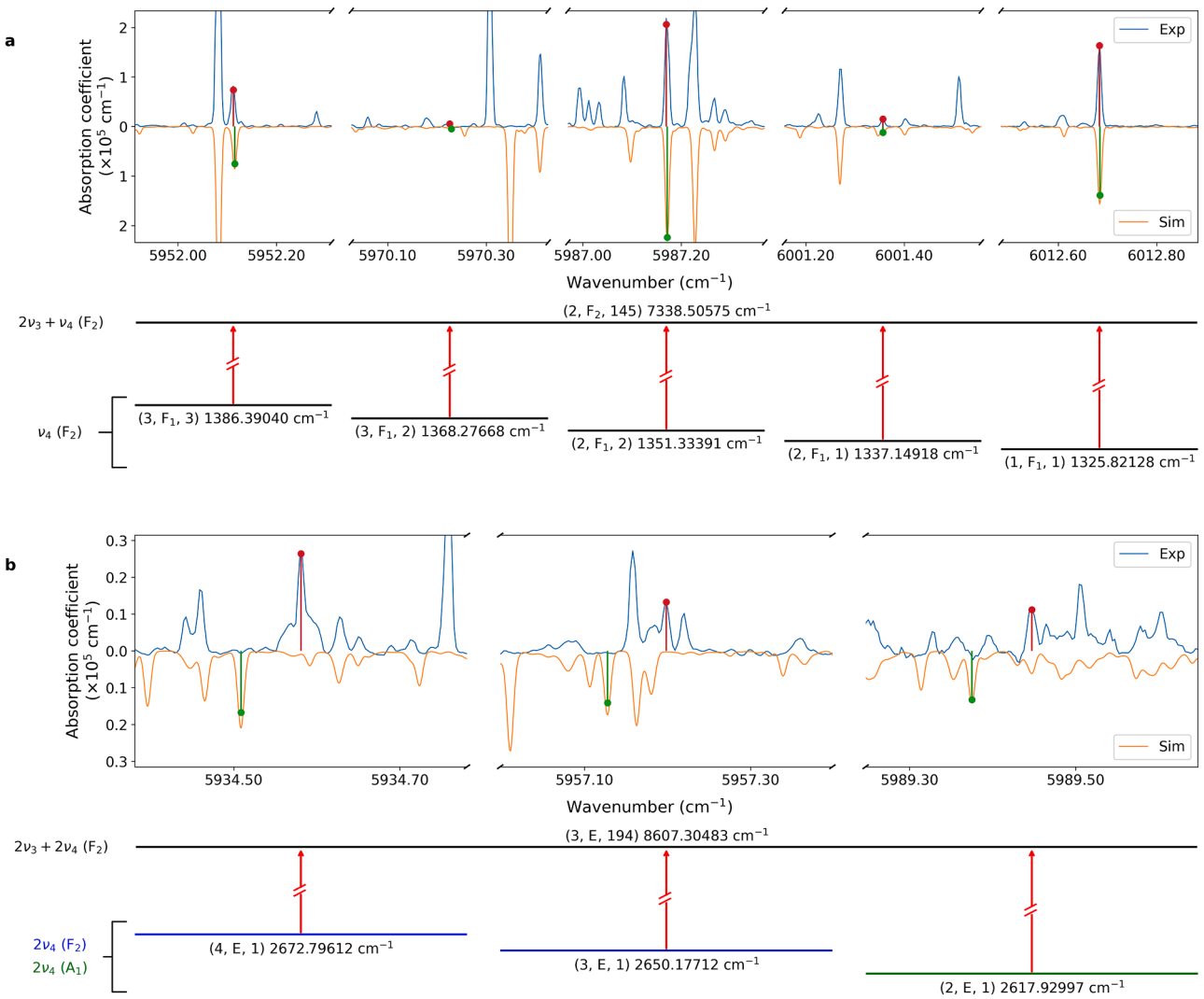

Fig. 7. Group of lines identified using the LSCD method. The rovibrational energy levels are labeled using the notation (J, C, n), where J is the quantum number relative to the total angular momentum, C the symmetry, and n the multiplicity index. In panel (b), the systematic shift between the positions of the calculated and experimental lines indicates that the position of the rovibrational level $(3, E, 194)$ is underestimated by 0.07 cm^{-1}.

estimate the density of the isentropic core, while transitions with $J \geq 7$ were taken into account to estimate the average density of the shear layer. As a result, $n_{IC} = 3.16 \times 10^{15}$ cm^{-3} ($Q_{IC} = Q_{IC}^{rot} \times Q_{IC}^{vib} = 30.93 \times 1.48$) and $n_{SL} = 7.97 \times 10^{14}$ cm^{-3} ($Q_{SL} = Q_{SL}^{rot} \times Q_{SL}^{vib} = 800.73 \times 1.46$). Part of the simulated spectrum is shown in Fig. 6. As it can be seen from this figure, the agreement between calculated and observed lines is very good for certain lines, both in position and intensity, in particular for lines belonging to cold bands or hot bands associated with the dyad, while relatively large differences are observed for hot bands associated with higher polyads.

5. Spectrum analysis

Once the non-LTE spectrum has been simulated, line assignment can be carried out using a two-stage procedure. First, the experimental lines whose position and intensity are very close to the calculated lines are matched. In particular, this makes it possible to quickly identify the transitions of the cold bands and the hot bands that start from the dyad, which are calculated with a good accuracy by the effective model. A total of 1525 lines are identified at the end of this first stage. Second, a lower state combination difference (LSCD) procedure is systematically applied to identify series of transitions ending on a same upper rovibrational energy level (see examples given in Fig. 7). It is worth mentioning that up to the icosad range (polyad P_5), the line positions for low and medium J values in the EM have been corrected using experimental energy levels, as explained in Ref. [11]. The LSCD procedure is therefore reliable for assigning hot band transitions starting up to vibrational energy levels in the icosad. A total of 1000 lines are identified at the end of this second stage. All identified lines (stages 1 and 2) are listed in Table S1 of the supplementary material.

Specifically, the empirically refined theoretical line list was first restricted to the 16,789 transitions corresponding to calculated non-LTE integrated absorption coefficients ($\overline{\alpha}_{ij}^{cal}$) and non-LTE line amplitudes (H_{ij}^{cal}) greater or equal to the lowest integrated absorption coefficient and to the lowest line amplitude detected in our experimental spectrum (i.e. $\overline{\alpha}_{ij}^{cal} \geq 1.17\ 10^{-10}$ cm^{-2} and $H_{ij}^{cal} \geq 6.81\ 10^{-9}$ cm^{-1}). The first stage of the procedure is then applied with the following criteria: $|\widetilde{\nu}_{exp} - \widetilde{\nu}_{calc}| \leq 0.01$ cm^{-1} and $0.67\ H_{ij}^{cal} \leq H_{ij}^{exp} \leq 1.33\ H_{ij}^{cal}$. The second stage of the procedure begins with a systematic inventory of the transitions in the EM line list characterized by the same upper energy level. Transitions grouped in this way can be deduced from each other using LSCD. Our strategy is to simultaneously identify experimental transitions within the same group, consisting of 2 to 11 transitions (note that in the

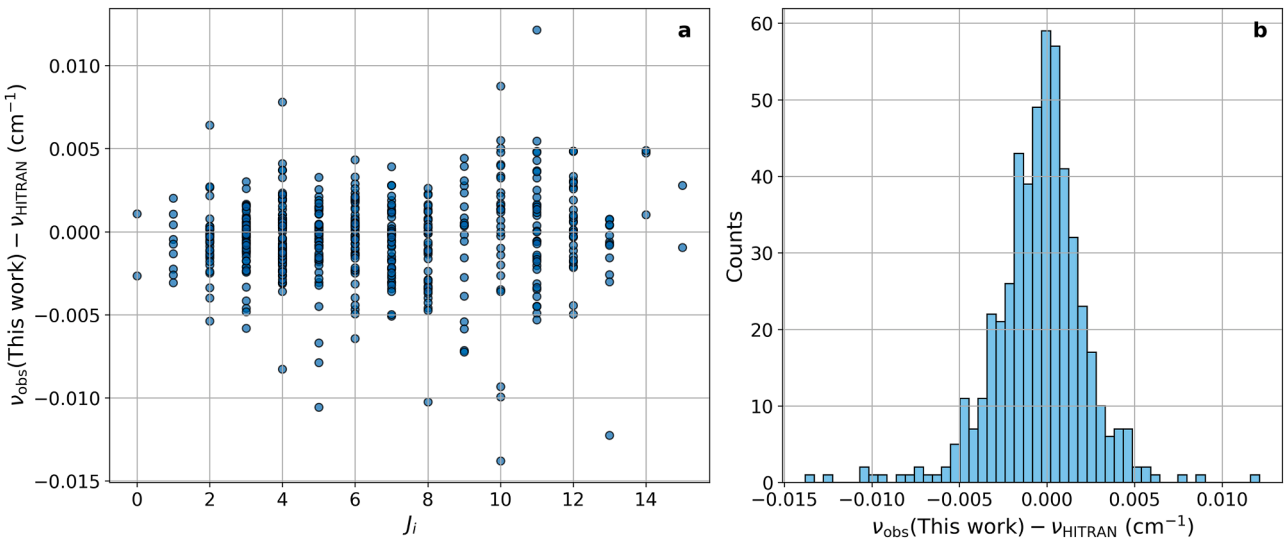

Fig. 8. Comparison of the position of the cold band transitions observed in this work with those listed in HITRAN 2020. Panel (a): Comparison for each lower ro-vibrational quantum number J_i. Panel (b): Histogram.

case of a single transition within a group, only the first stage is applied). The theoretical lines of the selected group are compared with the experimental lines within a reasonable range $|\widetilde{\nu}_{exp} - \widetilde{\nu}_{calc}| \leq 1$ cm^{-1} which corresponds to the greatest estimated inaccuracy in the calculations of the EM. The simultaneous identification is validated if $|\widetilde{\nu}_{\exp} - \widetilde{\nu}_{calc}| \leq 0.005$ cm^{-1} and $0.67\ H_{ij}^{cal} \leq H_{ij}^{exp} \leq 1.33\ H_{ij}^{cal}$ for each line within the group. It should be noted that whenever possible (i.e. when at least two transitions end on the same upper energy level), line identification in the first stage was confirmed by LSCD. Two examples are given in Fig. 7.

Table S2 of the supplementary information systematically compares our line assignments with the transitions reported in the latest version of the HITRAN database [39]. Within the spectral range investigated in this work (5880–6220 cm^{-1}), all the 4787 lines listed in HITRAN correspond to cold bands. The 1807 hot band transitions identified in this study are new and not reported in HITRAN 2020. A total of 718 cold-band transitions is observed in this work. Of the 4787 cold-band lines listed in HITRAN and originating from the WKLMC line list [25], only 110 are fully identified with the vibrational and ro-vibrational quantum numbers of the lower and upper energy levels. Among these 110 identified transitions, 52 are confirmed by our analysis, while some others are not observed as they were out of our experimental spectral coverage. For the remaining 666 cold-band transitions, our analysis specifies the upper vibrational state in many cases (for instance, the line at 5884.4657 cm^{-1}), the upper vibrational and ro-vibrational states (e.g., the line at 5884.6358 cm^{-1}), or even both the lower and upper vibrational and ro-vibrational states (e.g., the line at 5885.0490 cm^{-1}). Importantly, we also identified the lower ro-vibrational energy, which could not be systematically determined using the 2T method employed in ref [25]. In Fig. 8, the position of the cold band transitions observed in this work are compared with those listed in HITRAN 2020. Panels (a) and (b) reveal a distribution well centered around 0 and a root mean square (RMS) of 0.0027 cm^{-1}. It is worth noting that the accuracy of the line positions in WKMC [24] and WKLMC [25] databases is estimated to be 0.001 cm^{-1}. Therefore, the origin of the RMS highlighted in Fig. 8b is most likely due to a greater uncertainty in the line positions measured in Rennes.

6. Conclusion

Preheating methane before cooling it by supersonic expansion offers a number of advantages for studying its infrared spectrum. Above all, this approach simplifies the rotational structure of the spectrum, which is extremely complex at high temperatures, while maintaining the population of certain excited vibrational states, making it possible to analyze a large number of hot band transitions. Our spectrum analysis confirmed a fast V-V relaxation within vibrational polyads and a much slower relaxation between different polyads. This results in an accumulation of the population on the first vibrational states of each polyad, namely ν_2 and ν_4 for the dyad (P_1), $2\nu_4$ for the pentad (P_2), $3\nu_4$ for the octad (P_3). The low divergence of the flow imposed by the use of a Laval nozzle combined with a very low translational temperature also leads to reduced line widths, which reduces line superposition and greatly facilitates spectrum analysis.

The line list produced by the effective model was used extensively to determine the rotational and vibrational temperatures of the flow, allowing a rigorous simulation of our non-LTE spectrum. Based on this simulation and the method of lower state combination differences, we identified 718 cold band transitions and 1807 hot band transitions involving lower vibrational states of the dyad, pentad and octad among the 6088 observed lines. The position agreement of the lines calculated by the EM is very good for cold bands and hot bands from the dyad (80 % of the assigned lines from GS and dyad correspond to $|O-C| \leq 0.006$ cm^{-1} and $|O-C| \leq 0.008$ cm^{-1}, respectively) and not as good for hot bands from higher polyads (80 % of the assigned lines from pentad and octad correspond to an $|O-C| \leq 0.260$ cm^{-1} and $|O-C| \leq 0.308$ cm^{-1}, respectively).

These new experimental data will be used to improve the accuracy of the effective model by refining a set of parameters. From an experimental point of view, a planar Laval nozzle is currently being tested to limit the impact of boundary layers on the spectrum while increasing the absorption length through the isentropic core of the flow.

CRediT authorship contribution statement

Lyam Rolland-Roignant: Software, Methodology, Formal analysis. **Eszter Dudás:** Investigation. **Nicolas Suas-David:** Writing – review & editing, Investigation. **Michaël Rey:** Funding acquisition, Data curation. **Samir Kassi:** Investigation. **Andrei V. Nikitin:** Data curation. **Robert Georges:** Writing – original draft, Supervision, Project administration, Funding acquisition, Conceptualization.

Declaration of competing interest

Robert Georges reports financial support was provided by French

National Research Agency. Michael Rey reports financial support was provided by French National Research Agency. If there are other authors, they declare that they have no known competing financial interests or personal relationships that could have appeared to influence the work reported in this paper.

Acknowledgments

The French National Research Agency is gratefully acknowledged for its support for the FULLDIBS project (grant ANR-20-CE31–0014) and the TEMMEX project (grant ANR-21–30CE-0053–01). This work was supported by the Thematic Actions “Physique et Chimie du Milieu Interstellaire” (PCMI) and "Physique Stellaire" of INSU Programme National “Astro”, with contributions from CNRS Physique & CNRS Chimie, CEA, and CNES. Julien Cartron is thanked for his help in analyzing the data.

Supplementary materials

Supplementary material associated with this article can be found, in the online version, at doi:10.1016/j.jqsrt.2025.109656.

Appendix A. Supplementary material

Table S1. List of methane rovibrational transitions assigned between 5880 and 6220 cm^{-1}.

Table S2. Comparison of methane lines observed in this work with those listed in HITRAN 2020.

Data availability

Data will be made available on request.

References

[1] Miles BE, Biller BA, Patapis P, Worthen K, Rickman E, Hoch KKW, et al. The JWST early-release Science Program for Direct Observations of Exoplanetary Systems II: a 1 to 20 μm spectrum of the planetary-mass companion VHS 1256–1257 b. Astrophys J Lett 2023;946:L6. https://doi.org/10.3847/2041-8213/acb04a.

[2] Chubb KL, Robert S, Sousa-Silva C, Yurchenko SN, Allard NF, Boudon V, et al. Data availability and requirements relevant for the Ariel space mission and other exoplanet atmosphere applications. RAS Tech Instrum 2024;3:636–90. https://doi.org/10.1093/rasti/rzae039.

[3] Barman TS, Konopacky QM, Macintosh B, Marois C. SIMULTANEOUS DETECTION OF WATER, METHANE, AND CARBON MONOXIDE IN THE ATMOSPHERE OF EXOPLANET HR 8799 b. Astrophys J 2015;804:61. https://doi.org/10.1088/0004-637X/804/1/61.

[4] Guilluy G, Sozzetti A, Brogi M, Bonomo AS, Giacobbe P, Claudi R, et al. Exoplanet atmospheres with GIANO - II. Detection of molecular absorption in the dayside spectrum of HD 102195b. Astron Astrophys 2019;625:A107. https://doi.org/10.1051/0004-6361/201834615.

[5] Tinetti G, Encrenaz T, Coustenis A. Spectroscopy of planetary atmospheres in our Galaxy. Astron Astrophys Rev 2013;21:63. https://doi.org/10.1007/s00159-013-0063-6.

[6] Swain MR, Vasisht G, Tinetti G. The presence of methane in the atmosphere of an extrasolar planet. Nature 2008;452:329–31. https://doi.org/10.1038/nature06823.

[7] Swain MR, Tinetti G, Vasisht G, Deroo P, Griffith C, Bouwman J, et al. Water, methane, and carbon dioxide present in the dayside spectrum of the exoplanet HD 209458b. Astrophys J 2009;704:1616–21. https://doi.org/10.1088/0004-637X/704/2/1616.

[8] Tinetti G., Deroo P., Swain M.R., Griffith C.A., Vasisht G., Brown L.R., et al. PROBING THE TERMINATOR REGION ATMOSPHERE OF THE HOT-JUPITER XO-1b WITH TRANSMISSION SPECTROSCOPY. Astrophys J 2010;712:L139–42. https://doi.org/10.1088/2041-8205/712/2/L139.

[9] Swain M.R., Deroo P., Griffith C.A., Tinetti G., Thatte A., Vasisht G., et al. A ground-based near-infrared emission spectrum of the exoplanet HD 189733b Nature 2010;463:637–9. https://doi.org/10.1038/nature08775.

[10] Waldmann I.P., Tinetti G., Drossart P., Swain M.R., Deroo P., Griffith C.A. Ground-based near-infrared emission spectroscopy of hd 189733b Astrophys J 2011;744:35. https://doi.org/10.1088/0004-637X/744/1/35.

[11] Rey M., Nikitin A.V., Bézard B., Rannou P., Coustenis A., Tyuterev V.G. New accurate theoretical line lists of 12CH4 and 13CH4 in the 0–13400 cm−1 range: application to the modeling of methane absorption in Titan’s atmosphere. Icarus 2018;303:114–30. https://doi.org/10.1016/j.icarus.2017.12.045.

[12] Rey M., Nikitin A.V., Tyuterev V.G. Accurate theoretical methane line lists in the infrared up to 3000 K and quasi-continuum absorption/emission modeling for astrophysical applications. Astrophys J 2017;847:105. https://doi.org/10.3847/1538-4357/aa8909.

[13] Rey M., Nikitin A.V., Babikov Y.L., Tyuterev V.G. TheoReTS – An information system for theoretical spectra based on variational predictions from molecular potential energy and dipole moment surfaces. J Mol Spectrosc 2016;327:138–58. https://doi.org/10.1016/j.jms.2016.04.006.

[14] Yurchenko S.N., Tennyson J. ExoMol line lists – IV. The rotation–vibration spectrum of methane up to 1500 K. Mon Not R Astron Soc 2014;440:1649–61. https://doi.org/10.1093/mnras/stu326.

[15] Yurchenko S.N., Amundsen D.S., Tennyson J., Waldmann I.P. A hybrid line list for CH4 and hot methane continuum. Astron Astrophys 2017;605:A95. https://doi.org/10.1051/0004-6361/201731026.

[16] Hargreaves R.J., Gordon I.E., Rey M., Nikitin A.V., Tyuterev V.G., Kochanov R.V., et al. An accurate, extensive, and practical line list of methane for the HITEMP database. Astrophys J Suppl Ser 2020;247:55. https://doi.org/10.3847/1538-4365/ab7a1a.

[17] Rey M. Novel methodology for systematically constructing global effective models from ab initio-based surfaces: a new insight into high-resolution molecular spectra analysis. J Chem Phys 2022;156:224103. https://doi.org/10.1063/5.0089097.

[18] Hjältén A., Silva de Oliveira V., Silander I., Rosina A., Rey M., Rutkowski L., et al. Measurement and assignment of J = 5 to 9 rotational energy levels in the 9070–9370 cm−1 range of methane using optical frequency comb double-resonance spectroscopy. J Chem Phys 2024;161:124311. https://doi.org/10.1063/5.0223447.

[19] Nikitin A.V., Rodina A.A., Protasevich A.E., Manceron L., Rey M., Tyuterev V.G. New quantum assignments and analysis of high-resolution H212CO spectra in the range 3700–4450 cm−1. J Quant Spectrosc Radiat Transf 2024;329:109180. https://doi.org/10.1016/j.jqsrt.2024.109180.

[20] Khan M.V., Jacquemart D., Guinet M., Rey M., Nikitin A.V. Line list for the ν_3, $\nu_3+\nu_6-\nu_6$ and $2\nu_3-\nu_3$ bands of methyl fluoride at 9.5 μm. J Quant Spectrosc Radiat Transf 2025;345:109525. https://doi.org/10.1016/j.jqsrt.2025.109525.

[21] Georges R., Herman M., Hilico J.-.C., Robert O. High-resolution FTIR spectroscopy using a jet: sampling the rovibrational spectrum of 12CH4. J Mol Spectrosc 1998;187:13–20. https://doi.org/10.1006/jmsp.1997.7462.

[22] V Nikitin A., Boudon V., Wenger C., Albert S., R Brown L., Bauerecker S., et al. High resolution spectroscopy and the first global analysis of the Tetradecad region of methane 12CH4. Phys Chem Chem Phys 2013;15:10071–93. https://doi.org/10.1039/C3CP50799H.

[23] Gao B., Kassi S., Campargue A. Empirical low energy values for methane transitions in the 5852–6181 cm−1 region by absorption spectroscopy at 81K. J Mol Spectrosc 2009;253:55–63. https://doi.org/10.1016/j.jms.2008.09.005.

[24] Campargue A., Leshchishina O., Wang L., Mondelain D., Kassi S., Nikitin A.V. Refinements of the WKMC empirical line lists (5852–7919 cm−1) for methane between 80 K and 296 K. J Quant Spectrosc Radiat Transf 2012;113:1855–73. https://doi.org/10.1016/j.jqsrt.2012.05.011.

[25] Campargue A., Leshchishina O., Wang L., Mondelain D., Kassi S. The WKLMC empirical line lists (5852–7919 cm−1) for methane between 80 K and 296 K: “final” lists for atmospheric and planetary applications. J Mol Spectrosc 2013;291:16–22. https://doi.org/10.1016/j.jms.2013.03.001.

[26] Campargue A., Leshchishina O., Mondelain D., Kassi S., Coustenis A. An improved empirical line list for methane in the region of the $2\nu_3$ band at 1.66 μm. J Quant Spectrosc Radiat Transf 2013;118:49–59. https://doi.org/10.1016/j.jqsrt.2012.12.004.

[27] Votava O., Kassi S., Campargue A., Romanini D. Comb coherence-transfer and cavity ring-down saturation spectroscopy around 1.65 μm: kHz-accurate frequencies of transitions in the $2\nu_3$ band of 12CH4. Phys Chem Chem Phys 2022;24:4157–73. https://doi.org/10.1039/D1CP04989E.

[28] Ghysels M., Vasilchenko S., Mondelain D., Béguier S., Kassi S., Campargue A. Laser absorption spectroscopy of methane at 1000 K near 1.7 μm: a validation test of the spectroscopic databases. J Quant Spectrosc Radiat Transf 2018;215:59–70. https://doi.org/10.1016/j.jqsrt.2018.04.032.

[29] Wong A., Bernath P.F., Rey M., Nikitin A.V., Tyuterev V.G. Atlas of experimental and theoretical high-temperature methane cross sections from T = 295 to 1000 K in the near-infrared. Astrophys J Suppl Ser 2019;240:4. https://doi.org/10.3847/1538-4365/aaed39.

[30] Foltynowicz A., Rutkowski L., Silander I., Johansson A.C., Silva de Oliveira V., Axner O., et al. Sub-doppler double-resonance spectroscopy of methane using a frequency comb probe. Phys Rev Lett 2021;126:063001. https://doi.org/10.1103/PhysRevLett.126.063001.

[31] Foltynowicz A., Rutkowski L., Silander I., Johansson A.C., Silva de Oliveira V., Axner O., et al. Measurement and assignment of double-resonance transitions to the 8900–9100 cm−1 levels of methane. Phys Rev A 2021;103:022810. https://doi.org/10.1103/PhysRevA.103.022810.

[32] Louviot M., Suas-David N., Boudon V., Georges R., Rey M., Kassi S. Strong thermal nonequilibrium in hypersonic CO and CH4 probed by CRDS. J Chem Phys 2015;142:214305. https://doi.org/10.1063/1.4921893.

[33] Dudás E., Suas-David N., Brahmachary S., Kulkarni V., Benidar A., Kassi S., et al. High-temperature hypersonic laval nozzle for non-LTE cavity ringdown spectroscopy. J Chem Phys 2020;152:134201. https://doi.org/10.1063/5.0003886.

[34] Dudás E., Vispoel B., Gamache R.R., Rey M., Tyuterev V.G., Nikitin A.V., et al. Non-LTE spectroscopy of the tetradecad region of methane recorded in a hypersonic flow. Icarus 2023;394:115421. https://doi.org/10.1016/j.icarus.2022.115421.

[35] Suas-David N., Kulkarni V., Benidar A., Kassi S., Georges R. Line shape in a free-jet hypersonic expansion investigated by cavity ring-down spectroscopy and

computational fluid dynamics. Chem Phys Lett 2016;659:209–15. https://doi.org/10.1016/j.cplett.2016.06.082.

[36] Bruggeman P.J., Sadeghi N., Schram D.C., Linss V. Gas temperature determination from rotational lines in non-equilibrium plasmas: a review. Plasma Sources Sci Technol 2014;23:023001. https://doi.org/10.1088/0963-0252/23/2/023001.

[37] Laraia A.L., Gamache R.R., Lamouroux J., Gordon I.E., Rothman L.S. Total internal partition sums to support planetary remote sensing. Icarus 2011;215:391–400. https://doi.org/10.1016/j.icarus.2011.06.004.

[38] Gamache R.R., Vispoel B., Rey M., Tyuterev V., Barbe A., Nikitin A., et al. Partition sums for non-local thermodynamic equilibrium conditions for nine molecules of importance in planetary atmospheres. Icarus 2022:114947. https://doi.org/10.1016/j.icarus.2022.114947.

[39] Gordon I.E., Rothman L.S., Hargreaves R.J., Hashemi R., Karlovets E.V., Skinner F. M., et al. The HITRAN2020 molecular spectroscopic database. J Quant Spectrosc Radiat Transf 2022;277:107949. https://doi.org/10.1016/j.jqsrt.2021.107949.